



Hemodynamic analysis of bifurcated carotid artery morphologies at different physiological conditions

Nur Amani Hanis Roseman ¹, Ishkrizat Taib ^{1*}, Norfrizalidris Darlis ², Ahmad Mubarak Tajul Arifin ¹, Nor Adrian Nor Salim ¹, Awaludin Martin ³, Feblil Huda ³, Takahisa Yamamoto ⁴

¹Faculty of Mechanical and Manufacturing Engineering, Universiti Tun Hussein Onn Malaysia, 864000 Parit Raja, Batu Pahat, Johor, MALAYSIA.

²Faculty of Engineering Technology, Universiti Tun Hussein Onn Malaysia, Hab Pendidikan Tinggi, Pagoh, KM 1, Jalan Panchor, 84600 Panchor, Johor, MALAYSIA.

³Faculty of Mechanical Engineering, Universitas Riau, Pekanbaru, Riau 28293, INDONESIA.

⁴Department of Mechanical Engineering, National Institute of Technology, Gifu College, 2236-2 Kamimakuwa, Motosu 501-0495, JAPAN.

*Corresponding author: iszat@uthm.edu.my

KEYWORDS	ABSTRACT
Carotid artery Morphology Dolicoarteriopathies Thrombosis CFD	This study was conducted to determine the haemodynamic behavior of different carotid artery morphologies. Six different carotid artery morphologies were constructed, and simulations through the use of the computational fluid dynamic (CFD) method performed under two physiological conditions; normal (NBP) and high blood pressure (HBP). The haemodynamic behavior was evaluated using several parameters in understanding the wear and tear on the vascular lining, including time-averaged wall shear stress (TAWSS), time-averaged wall shear stress gradient (TAWSSG), oscillatory shear index (OSI) and relative residence time (RRT). Based on the observation, structural irregularities at the contributed to potential surface-wall stress, influencing the overall distribution of hemodynamic parameters. Both HBP and NBP showed similar area of hemodynamic parameters' distribution with HBP exhibited a higher rate for high shear stress thrombosis. Therefore, vascular geometry as well as the physiological conditions presented has significant effect on the blood flow behavior leading to potential thrombosis development.

Received 25 September 2024; received in revised form 8 January 2025; accepted 31 January 2025.

To cite this article: Roseman et al., (2025). Hemodynamic analysis of bifurcated carotid artery morphologies at different physiological conditions. *Jurnal Tribologi* 45, pp.242-267

1.0 INTRODUCTION

The obstruction of the carotid artery is significantly connected with one-third of stroke incidences in the world (Everson-Rose & Fordham, 2022). Severe luminal narrowing of the carotid artery contributes to transient ischemic attack events due to momentary blockage of blood delivery to a region or section of the brain and eventually increases the rate of morbidity as well as mortality of patients (Huang *et al.*, 2024). The occurrences of carotid artery occlusion happened due to the contribution of numerous pathophysiological factors, including the development of atherosclerosis and thrombus formation in the blood vessels (Campbell *et al.*, 2019). Atherosclerotic plaque deposit is controlled or influenced by vascular fluid dynamics in which the friction between blood flow and the vascular wall depicts a critical role (Sjöstrand *et al.*, 2023). The generated shear forces produce from the interaction of blood and vessel lining affect the formation of thrombosis plaque. The disturbed blood flow due to structural irregularities may increase friction and reduced shear stress which further promote the formation of plaques. The vascular morphologies elevated the resistance within the flow, thus potentially aggravating the development of thrombus. These will lead to a cycle of elevated friction, further plaque deposition and consequently narrowing the arterial lumen (Carvalho *et al.*, 2021). Previous studies reported on the numbers of carotid artery geometry variations or abnormalities found either due to normal ageing progression or diseases. The severity of carotid artery morphologies anomalies affected the degree of haemodynamic disturbances (Carallo, 2019)

As vascular geometry has been recognized and proven to have a significant influence on blood flow behavior, understanding vascular geometry and its geometric properties while linking it to a specific clinical condition might provide insight into the mechanism in the evolution of illness (Pinho *et al.*, 2019). In the carotid arteries, specific structural and anatomical abnormalities presented are known as dolichoarteriopathies (DA) which has long piqued curiosity among the non-atheromatous alteration disease. Both normal ageing progression and the development of diseases have been associated with geometric changes and alterations of the artery. However, whether DA triggering is prompt due to diseases or is just a result of remodelling throughout the ageing process is still uncertain (Beigelman *et al.*, 2014). DA is commonly exhibited by the internal carotid artery (ICA) and has been investigated intensively in numerous studies (Iomini *et al.*, 2024; Balevi, 2020).

The earliest classification of DA variation was conducted by Zhong *et al.*, (1985) which used the curvature and planarity of carotid artery siphon bend to and then definitively established four types of shapes which are U-shape, V-shape, C-shape, and S-shape [27, 28]. Furthermore, Weibel *et al.*, (1965a), Weibel *et al.*, (1965b) and Metz *et al.*, (1961) initially characterized DA basically with the abnormal elongation presented by the ICA. They established DA into three types: tortuosity, coiling, and kinking. Type 1-tortuosity is formed with a curved stretch, elongation, and undulation through an angulation of more than ninety degrees ($>90^\circ$). Thus, tortuosity developed a loop and presumed the S and C-shape of the artery. Besides, type 2-coiling or loop is described with an angulation of 360° on the artery transversal axis. Coiling may result in the formation of C, S, and U-shaped artery structures. In addition, type 3-kinking presented with two or more segments in the carotid artery diverging and bending with an internal angle of ninety degrees or less ($\leq 90^\circ$) (Beigelman *et al.*, 2014; Weibel *et al.*, 1965b).

As more study on DA progresses, the categorization of the morphology of the carotid artery eventually divided into four types using the angle of deviation from the vertical axis. Kinking in ICA was determined as the most common morphological anomaly (Di Pino *et al.*, 2021). Conversely, a study done by Nagata *et al.*, (2016) by analysing 296 arteries of patients determined

the prevalence of tortuosity to have the highest occurrences in carotid arteries, followed by straight, coiling, and kinking. Moreover, it was found that tortuosity and straightness of arteries have similar frequencies to take place on both the left and the right sides.

DA of the carotid artery correlated with intimal proliferation, atherosclerotic plaque, and stenosis resulting in haemodynamic changes, which are primarily dependent on the internal surface of the vascular wall along with the value of the angle of the smooth curve of the arterial siphon (Iomini *et al.*, 2024). The comparatively intricate geometry surrounding curves and out-of-plane bends have a vital element in atherogenesis thus, providing a significant influence on the haemodynamic performance in the carotid artery (DiCarlo, 2018). The intricacy of blood flow patterns *in vivo* was highlighted by Pedley (2022), which found that both pulsatile flow and structural changes in vessels affected the blood flow dynamically. Blood velocity is larger along the outside wall of a vessel's curvature than along the inside wall when it curves, whereas the blood flow is slowest outside the wall and fastest near the flow divider when a vessel bifurcates. These complicated changes in blood velocity can result in large changes in WSS both along the blood vessel's length and around its circumference.

Thought on the haemodynamic flow helps in the development of biomedical equipment for effective treatments (Hidayat *et al.*, 2023). Numerical simulations using the computational fluid dynamics (CFD) method can be used to analyse the fluid flow behavior (Zulkifli *et al.*, (2023); Ghani *et al.*, (2023). CFD provides a means of analysing haemodynamic disturbances of carotid artery morphologies *in vivo* quantitatively. Several haemodynamic parameters have been extensively discussed to be useful in predicting thrombosis development. These included the wall shear stress (WSS), time-averaged wall shear stress magnitude (TAWSS), time-averaged wall shear stress gradient (TAWSSG), oscillatory shear index (OSI) and relative residence time (RRT), which were proven to be substantial in conferring atherosclerosis related cases (Paisal *et al.*, 2019). Specific range values of each haemodynamic parameter reported in previous studies signify atherosclerotic activity (Rabbi, Laboni, & Arafat, 2020; Paisal *et al.*, 2019). Therefore, this study looked into the haemodynamic disturbances induced by morphological variations in the carotid artery to the blood flow at different physiological conditions.

2.0 METHODOLOGY

2.1 Simplified Carotid Arteries Geometries

Simplified models were design based on a study by Nagata *et. al.*, (2016) which used three-dimensional computed tomography (3DCT) to scan, reconstructed and classified based on the morphology of carotid artery. The data extracted were translated into a simple schematic diagram, which served as a guide and reference for drawing the simplified models. The simplified models comprise all components of the carotid artery, including the CCA, carotid sinus (CS), ICA, and ECA. The complexity of abnormal arterial wall structure and tortuosity found were streamlined into six types of carotid artery morphologies. Thus, six carotid artery morphologies introduced by Nagata *et al.*, (2016) were drawn using computer-aided design software code SOLIDWORKS (Dassault Systèmes SolidWorks Corporation, Waltham, Massachusetts, United States) to resemble real carotid arteries as shown in Figure 1.

Figure 1 explained the distinction morphologies of the carotid artery. Type I exhibited the most seen carotid artery with a straight ICA (common CA morphologies) whilst Type II and III displayed two different tortuosities of ICA. However, Type IV, and Type V demonstrated two different ICA

coiling, and Type VI revealed the kinking geometry of ICA. Each morphology of the carotid artery exhibited ICA sinus and connected to the point of bifurcation. The dimension applied in constructing these models was derived from the studies performed by Datta and Rakesh (2010), as shown in Figure 2. The measurement of these carotid artery models was mostly similar regarding the CCA, ICA sinus, and ECA. The ICA measurement is tabulated in Table 1.

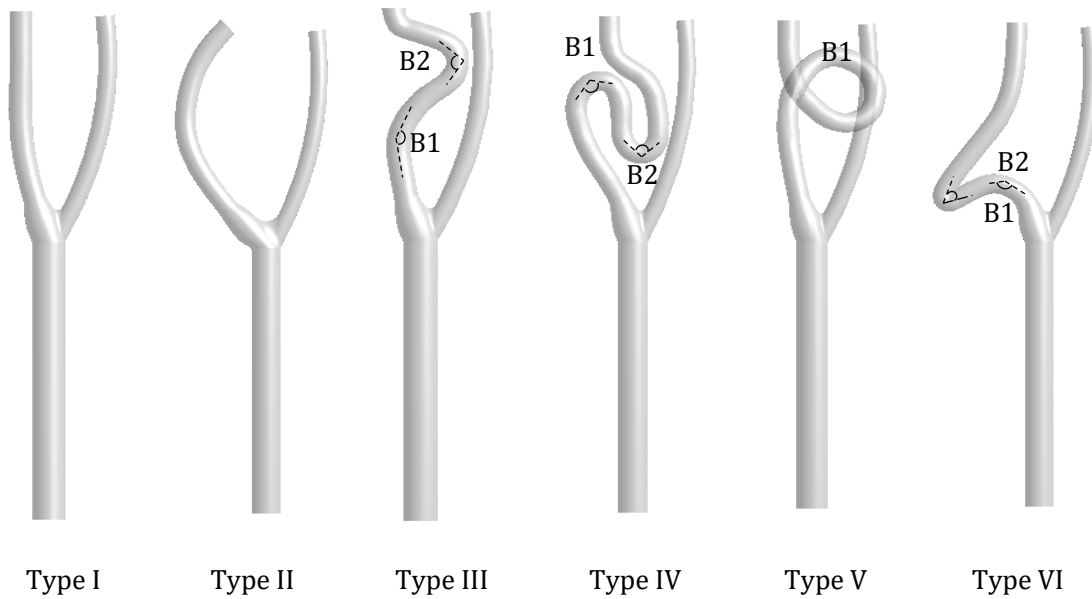


Figure 1: Carotid artery morphologies; Type I (Straight), Type II and Type III (Tortuous), Type IV and Type V (Coiling), Type VI (Kinking).

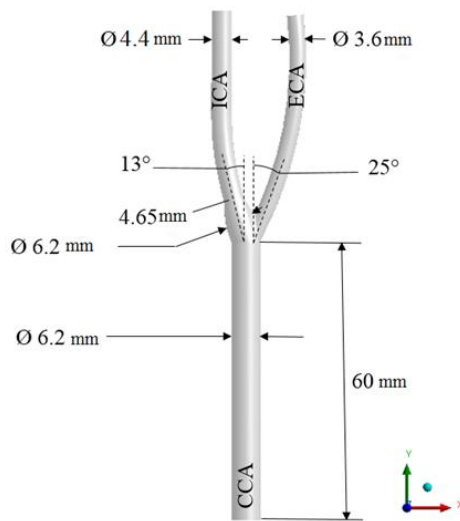


Figure 2: Type I straight carotid artery dimension.

Table 1: Measurement of the internal carotid artery for each model.

Carotid Artery Model	Angle CCA-ICA	Bend Angle ICA		Length ICA (mm)
		B1	B2	
Type I	13°	-	-	41.2
Type II	42°	-	-	45.8
Type III	13°	171°	134°	51.2
Type IV	13°	110°	100°	87.9
Type V	13°	360°	-	92.2
Type VI	13°	124°	48°	62.6

2.2 Discretization Techniques

The morphologies of the carotid artery have complex geometries and the suitable types of the mesh should be considered to generate the meaningful result. In this study, the patch conforming tetrahedron mesh method was employed for the discretization technique. This method was adept in producing precise meshing when involving geometry with complex configurations. The 'body sizing' feature was set to a minimum element size of 0.000209 m, and the 'inflation' feature was constructed with five layers near the carotid wall as illustrated in Figure 3.

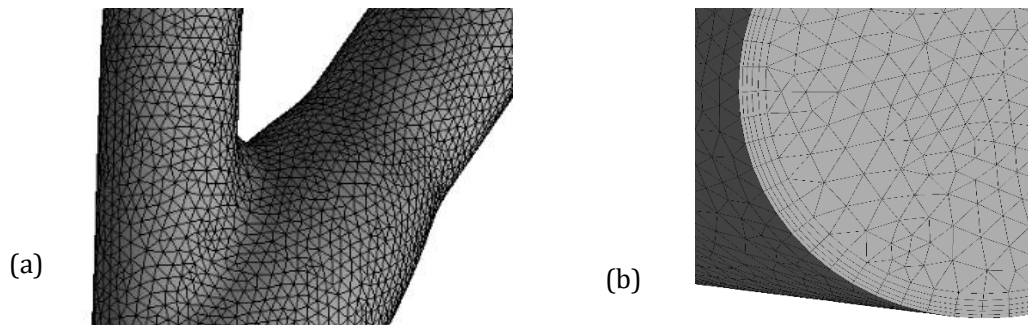


Figure 3: Meshing of carotid artery morphology with the effect of (a) body sizing and (b) inflation.

2.3 Parameter Assumption and Boundary Conditions

The carotid artery is located at the upper limb of the transverse aorta which supplies blood to the brain. The blood is normally considered as non-Newtonian fluid. However, in this study, the simulated blood was considered to be incompressible Newtonian fluid (Kumar *et al.*, 2020; Mendieta *et al.*, 2020) with blood density (ρ) of 1060 kg/m³ and viscosity (μ) of 0.0035 Pa s (Pal *et al.*, 2022). This consideration was made due to the calculation of the shear rate being more than 100 1/s. The calculated shear rate value more than 100 1/s is expected for the turbulence phenomenon which does not occur for the non-Newtonian. No-slip boundary condition was imposed along the rigid carotid arterial wall. The fluid mathematical viscous model was determined by calculating the Reynolds number (Re) (Sambu *et al.*, 2024). The Re number was derived from Equation (1) (Khalili, Gamage & Mansy, 2018) where D is diameter and V is velocity magnitude.

$$Re = \frac{(V.D.\rho)}{\mu} \tag{1}$$

With the Re number less than 2000 throughout the pulsatile flow, the fluid flow was considered laminar. Nevertheless, the current study involved complex morphologies of the carotid artery which resulted in the transition from laminar to turbulent flow (Saqr *et al.*, 2020). As a result, the turbulent viscous model was used instead of a laminar model. In addition, the shear stress transfer (SST) model was chosen from among the current turbulent models for its reliability in flow modelling near the artery wall (Yu, Tan & Wang, 2021; Santos *et al.*, 2021). The carotid artery model has one inlet and two outflows as depicted in Figure 4. The velocity at the inlet was considered using velocity waveforms obtained from experimental results in the study done by Azhim *et al.*, (2013) as shown in Table 2.

Table 2: Velocities of cardiac phases at different physiological conditions (Azhim *et al.*, 2013).

Cardiac Phase (Time, s)	Velocity under different physiological conditions (m/s)	
	NBP	HBP
End-diastolic (0.27)	0.1754	0.2177
Peak-systolic (0.36)	0.9553	0.9303
First incisura (0.46)	0.4855	0.6277
Second incisura (0.59)	0.2391	0.3183
Peak-diastolic (0.65)	0.3818	0.3848



Figure 4: Boundary conditions of carotid artery model.

Flow rate weighting was established for the outflow border condition in both ECA and ICA. A study done by Aldoori and Lee (1993) stated that the average flow rate in the CCA inlet was 420 mL/min, and the average flow rate in ICA was 276 mL/min. Therefore, the average flow rate in ECA calculated using the conservation of mass relation with Equation (2) was 144 mL/min.

Therefore, the appropriate weightage, (w), proceeded using Equation (3), resulting in a weighted ratio of 0.6571:0.3429 for ICA to ECA.

$$\sum_{in} \dot{V} = \sum_{out} \dot{V} \quad (2)$$

$$w = \frac{\dot{V}_{outlet}}{\dot{V}_{inlet}} \quad (3)$$

2.4 Computational Model and Governing Equations

ANSYS Fluent is used to solve the simulation of the carotid artery by utilizing finite volume (FVM). The continuity equation was applied to density of the blood (the intense attribute corresponding to mass), obtaining Equation (4). The equation of conversation of mass is as follows (Masibayi, 2011):

$$\frac{d\rho}{dt} + \nabla \cdot (\rho \vec{v}) = 0 \quad (4)$$

The density of blood is considered an incompressible fluid. The simplest form of the equation was obtained by setting the density derivative to zero and dividing by a constant. Thus, the governing continuity equation becomes Equations (5) and (6).

$$\rho \nabla \cdot \vec{v} = 0 \quad (5)$$

$$\nabla \cdot \vec{v} = 0 \quad (6)$$

Besides, the Navier-Stokes equation is applied with the assumption concerning the nature of the stress tensor, τ , forms the basis for Newtonian fluid equations. Stress is proportional to the rate of deformation in a Newtonian fluid (the change in velocity in the directions of the stress). That is to say, as follows in Equation (7).

$$\tau_{ij} = \mu \left(\frac{\partial u_i}{\partial x_j} + \frac{\partial u_j}{\partial x_i} \right) \quad (7)$$

The viscosity of the fluid indicates how easily it flows when subjected to body forces and is defined by the proportionality constant, μ . Furthermore, the Navier-Stokes equation uses the divergence of stress, $\nabla \cdot T$ and replaces the divergence with a vector Laplacian produced the Equation (8).

$$\nabla \cdot T = \mu \nabla^2 v \quad (8)$$

The equation for an incompressible Newtonian fluid with constant viscosity would be as written in Equation (9) (Masibayi, 2011).

$$\rho \frac{Dv}{Dt} = -\nabla p + \mu \nabla^2 v + \rho g \quad (9)$$

2.5 Hemodynamic Parameters of Carotid Artery

Several haemodynamic parameters were applied to evaluate the effect of morphological variation on the development of atherosclerosis prone regions in the carotid arterial wall.

2.5.1 Time Averaged Wall Shear Stress (TAWSS)

The frictional force exerted in the luminal endothelium by the circulating blood flow column per unit area is known as wall shear stress (WSS) (Sia *et al.*, 2019). WSS distribution was assessed along the artery wall to predict neointimal growth. Equation (10) is based on Poiseuille's law to measure the magnitude WSS value, where μ_d denotes the dynamic viscosity, Q is the blood flow rate, and r indicates the lumen radius (Roseman, 2023).

$$\tau_w = \frac{4\mu_d Q}{\pi r^3} \quad (10)$$

The WSS profiles could also be measured using Equation (11), where \vec{n} is a normal vector to a wall surface and $\vec{\tau}_{ij}$ is the fluid viscous stress tensor (Paisal, 2018).

$$|\vec{\tau}_w| = |\vec{n} \cdot \vec{\tau}_{ij}| \quad (11)$$

A lower value of WSS of less than 1 Pa pointed out the arterial regions susceptible to atherosclerosis development, whereas a higher value of WSS of more than 7 Pa implies areas prone to high shear thrombosis progression and a greater possibility of plaque erosion (Lagache *et al.*, 2021; Paisal *et al.*, 2019). The WSS ranges between 1 to 7 Pa displayed healthy vascular areas (Soares, Carvalho & Leite, 2021). Time-averaged WSS (TAWSS) are typically employed to determine the mean value signifying WSS for each pulsatile cardiac cycle in a transient instance as WSS was calculated to anticipate the variables for time-dependent flow. Accordingly, TAWSS was solved using Equation (12), where T represents the one full cardiac cycle, and dt denotes the small-time increment (Azar *et al.*, 2019).

$$TAWSS = \frac{1}{T} \int_0^T |\vec{\tau}_w| dt \quad (12)$$

2.5.2 Time Averaged Wall Shear Stress Gradient (TAWSSG)

The wall shear stress gradient (WSSG) is a measure of the spatial changes of WSS magnitude in the artery. Areas with a high WSSG value of more than 5000 Pa/m are correlated to increases in intimal hyperplasia occurrences, arterial wall permeability, and atheromatous plaque formation (Paisal *et al.*, 2019). WSSG can be measured as:

$$\alpha = \frac{\tau}{|\tau|} \quad (13)$$

$$\beta = n_a \times \alpha \quad (14)$$

$$\frac{\partial \tau}{\partial \alpha} = \nabla \tau \cdot \alpha \tag{15}$$

$$\frac{\partial \tau}{\partial \beta} = \nabla \tau \cdot \beta \tag{16}$$

$$WSSG = \sqrt{\left(\frac{\partial \tau}{\partial \alpha}\right)^2 + \left(\frac{\partial \tau}{\partial \beta}\right)^2} \tag{17}$$

Equations (13), (14), (15), (16), and (17) demonstrated that the computation of WSSG involved WSS derivatives in two directions: the blood flow direction (α) and normal to the direction (β). The gradient operator (∇) represent the partial derivative in coordinate directions, whereas the empirical parameter n_A indicates the normal to the surface area (Roseman, 2023). Consequently, the WSSG was calculated as TAWSSG since this study involves transient pulsatile blood flow. TAWSSG is defined in Equation (18), where T denotes the duration of the cardiac cycle (Paisal *et al.*, 2019).

$$TAWSSG = \frac{1}{T} \int_0^T |\overline{WSSG}| dt \tag{18}$$

2.5.3 Oscillatory Shear Index (OSI)

The oscillatory shear index (OSI) offers a marker of changes in the direction of shear forces throughout the cardiac cycle. This haemodynamic variable was employed to detect recirculating blood flow locations (Lopes *et al.*, 2020). The OSI value represented by the oscillatory WSS can range from 0 to 0.5. Therefore, a region with a high OSI value greater than 0.2 was predicted to provide a greater risk of atherosclerotic events and vice versa. Equation (19) defined the computed OSI (Roseman, 2023):

$$OSI = \frac{1}{2} \left(1 - \frac{\frac{1}{T} \int_0^T |\vec{\tau}_w| dt}{\frac{1}{T} \int_0^T |\vec{\tau}_w| dt} \right) \tag{19}$$

2.5.4 Relative Residence Time (RRT)

RRT revealed the residence time of atherogenic particles of the blood in contact with or close to the endothelium wall. This variable was proposed to determine plausible arterial regions of stagnation. RRT was dependent on TAWSS and OSI, thus showing its vital role in quantifying the prospect of the atherosclerotic event (Azar *et al.*, 2019). Platelet aggregation and adhesion are aided by extended residence durations or stagnant flow. Additionally, the longer the prothrombogenic proteins aggregated throughout the clotting process, the more feasible for them to remain in the same location resulting in the preservation of the thrombus (Azar *et al.*, 2019). RRT higher than 10 Pa⁻¹ showed greater atherogenic activity. Therefore, RRT is defined in Equation (20) as follows (Paisal *et al.*, 2019):

$$RRT = \frac{1}{(1 - 2 \times OSI) \times TAWSS} \tag{20}$$

3.0 RESULTS AND DISCUSSION

3.1 Grid Independence Test (GIT)

GIT was executed using velocity distribution to determine the appropriate mesh which would accommodate the complexity of geometry (Ibrahim *et al.*, 2024; Saufi *et al.*, 2023). The normalized relative error was considered throughout the GIT to estimate the numerical errors in the simulation. Simulations using different numbers of nodes between 200k to 800k were carried out. Figure 5 depicts the velocity distribution of blood flow in the computational carotid artery model from the inlet to the bifurcated region of the artery. The calculated normalized relative error provided less than 5% for all the sampled nodes. From the observation made, all sampled nodes ranging from 200k to 800k were deemed suitable to be used in this study. However, a high number of nodes resulted in an increase in computation time, whereas a smaller number of nodes affected the accuracy of simulation result (Ayasamy, 2025; Krishnamurthy, 2025). In this study, 609k nodes was selected as it provides an optimal compromise between delivering accurate result while maintaining a manageable computation time.

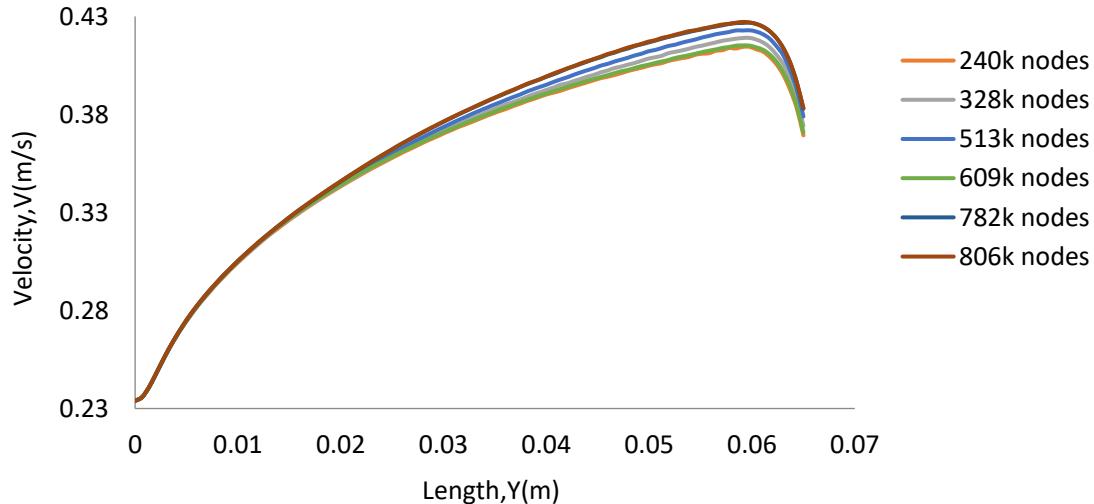


Figure 5: Velocity profile along center line carotid artery model for different number of nodes.

3.2 Experimental Validation of Numerical Simulation

Data validation was performed by comparing the carotid artery inlet velocity waveform at two different physiological conditions NBP and HBP, of the present study with experimental results executed by Azhim *et al.*, (2013) and is displayed in Figure 6. The average relative error calculated between present numerical data and experimental data for NBP and HBP were 2.11% and 2.97%, respectively. The percentage of relative error obtained showed a minimal discrepancy value. Thus, the result of the pulsatile inlet velocity waveform was relevant in these simulations.

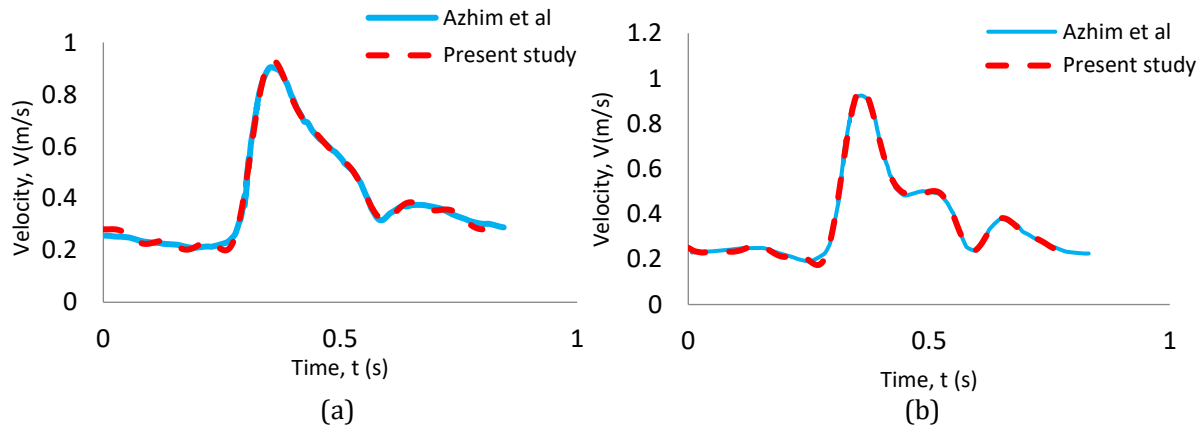


Figure 6: Comparison of velocity waveform in the common carotid artery of the present study with experimental data for two different physiological conditions; (a) NBP and (b) HBP.

3.3 Time Averaged Wall Shear Stress (TAWSS)

TAWSS_{low} distribution (blue) was revealed at the outer wall area of the carotid sinus, as shown in Figure 7 and Figure 8. This is similarly demonstrated in all the carotid artery morphology. The TAWSS_{low} distribution of the present study was consistent with a study by Yao *et al.* (2019) that revealed a comparable low shear stress region near the sinus in the carotid artery. Nevertheless, the Type II carotid artery morphology shows less TAWSS_{low} distribution at the sinus wall compared to other morphologies due to the difference in the angle of CCA-ICA. The increase in bifurcation angle in Type II decreases the TAWSS_{low} distribution. This is in agreement with Katakia *et al.*, (2022) which stated that the regions estimated for initial atheroma growth were more focalized as the bifurcation angle increases resulted in a decrease of TAWSS distribution. Atherogenesis activity increased when a significant portion of the luminal surface area was exposed to TAWSS_{low} distribution. This incidence was in line with Bir & Kelly (2022), which stated that disturbed blood flow regions provided apt conditions for the builds of atherosclerotic plaque.

TAWSS_{high} distribution (red) was more prominent at the point of bifurcation as well as at the curvature of each carotid morphology. Conversely, TAWSS_{low} distribution was observed at the inner wall of curvature. Hameed *et al.*, (2023) revealed that the blood flow recirculation formed proximate to the wall of bends and reduced the TAWSS at one side of the arterial bend. The TAWSS_{high} distribution more than 7 Pa is primarily responsible for determining which carotid artery morphology exhibits haemodynamic properties that favour the formation of high shear thrombosis (Soares, Carvalho & Leite, 2021; Lagache *et al.*, 2021; Kok *et al.*, 2019; Paisal *et al.*, 2019). Besides, a study by Kumar *et al.*, (2022) also presented high and low shear stress distribution due to the influence of curvature in the carotid artery proving the TAWSS distribution of the study was valid.

The carotid artery demonstrated similar regions of TAWSS_{low} and TAWSS_{high} distribution for both NBP and HBP conditions. Figure 9 and 10 illustrated the calculated percentage area coverage of both TAWSS_{low} (< 1 Pa) and TAWSS_{high} (> 7Pa) for better comparison. The percentage luminal surface area in HBP condition showed higher coverage distribution of TAWSS_{high} whereas the NBP condition exhibited a higher percentage value of TAWSS_{low}. The blood flow hitting the arterial walls and separating resulted in TAWSS_{high} regions, whereas flow recirculation generated the TAWSS_{low} region in the carotid artery. Type II presented the least TAWSS_{low} whereas Type I showed the least TAWSS_{high} at both NBP and HBP condition. On the other hand, Type IV

demonstrated the highest $TAWSS_{low}$ and Type V showed the highest percentage coverage of $TAWSS_{high}$. Thus, making Type IV and Type V prone to atherogenesis and high shear thrombosis, respectively.

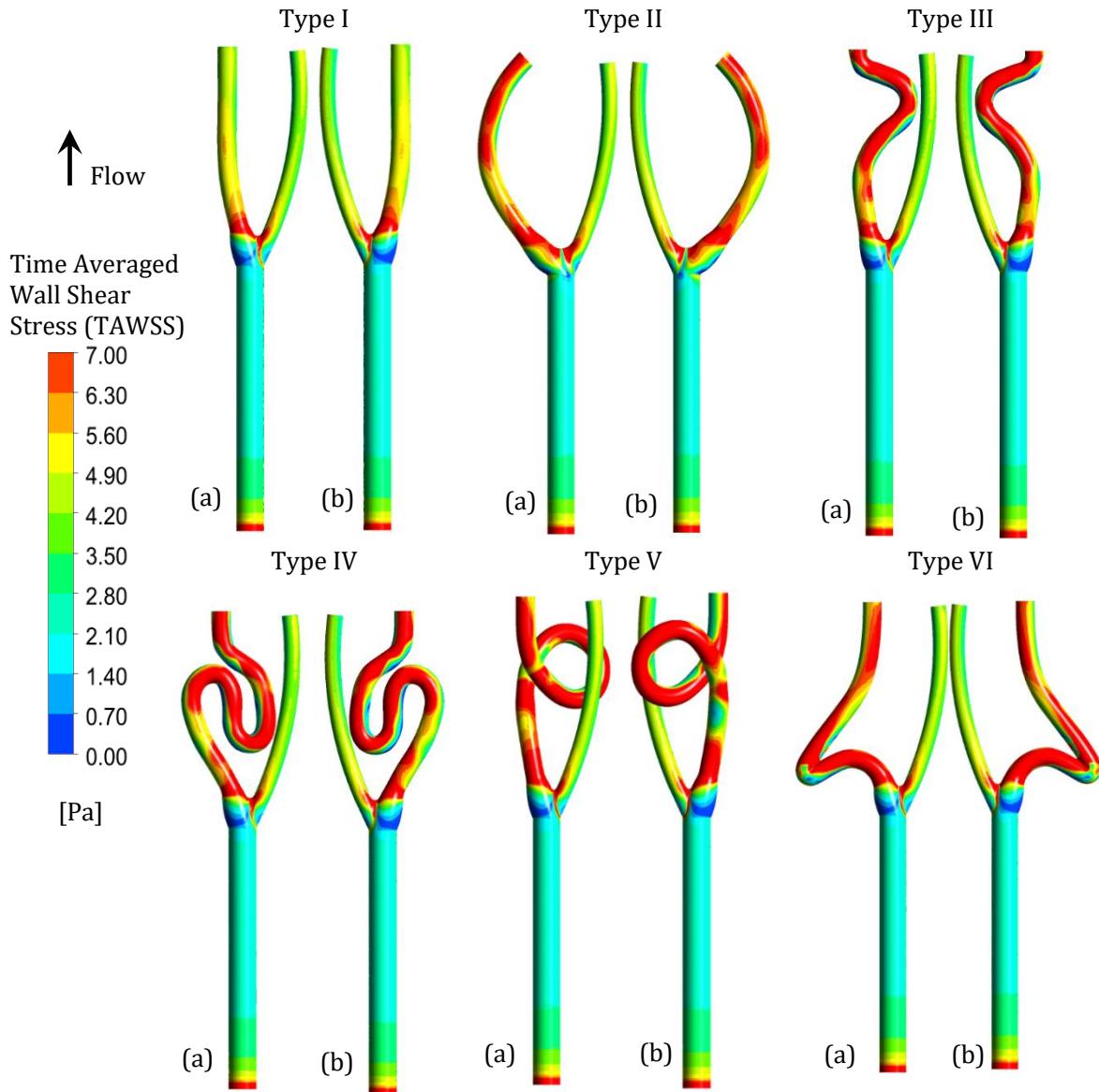


Figure 7: TAWSS distribution at (a) anterior (b) posterior of healthy carotid artery for NBP condition.

It is evident that the morphology and physiological state had an impact on the TAWSS distribution. Both NBP and HBP showed similar area of TAWSS distribution particularly at the bifurcation and curved areas of carotid artery. Yet, the NBP condition produced a more favorable

state for the formation of thrombosis and atherosclerosis due to higher $TAWSS_{low}$ distribution. In contrast, high shear thrombosis was expected to occur more during the HBP condition with higher $TAWSS_{high}$ distribution.

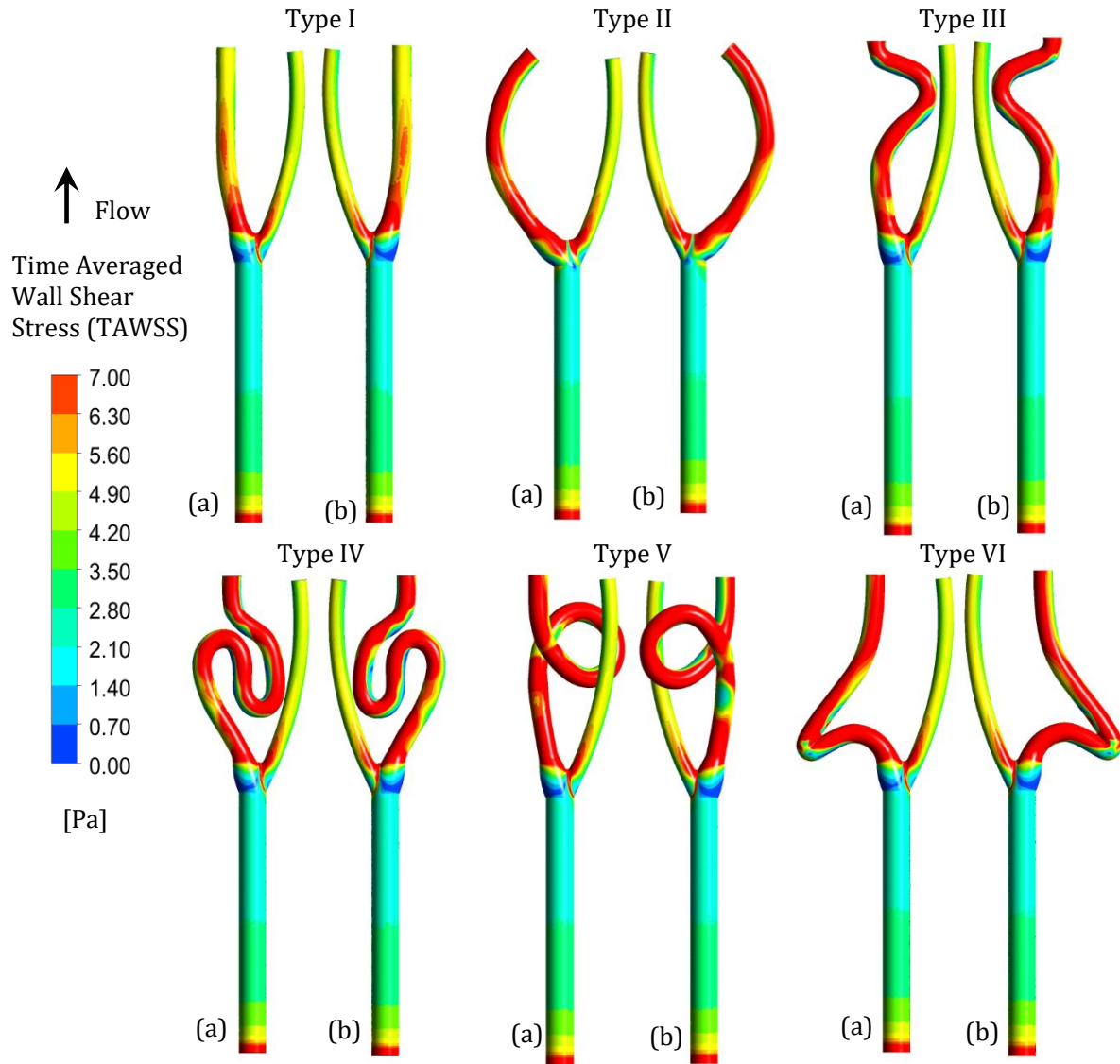


Figure 8: TAWSS distribution at (a) anterior (b) posterior of healthy carotid artery for HBP condition.

The results of the current investigation were consistent with a previous study done by Paisal *et al.*, (2019) that discovered a comparable pattern of TAWSS distribution in the stented carotid artery under different physiological situations.

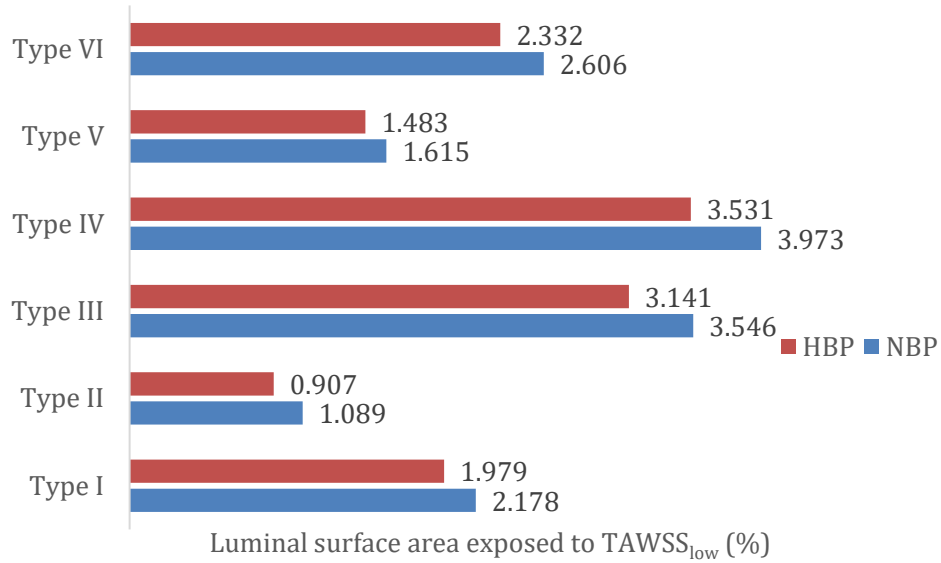


Figure 9: $TAWSS_{low}$ ($TAWSS < 1 \text{ Pa}$) distribution coverage to luminal surface area of carotid artery.

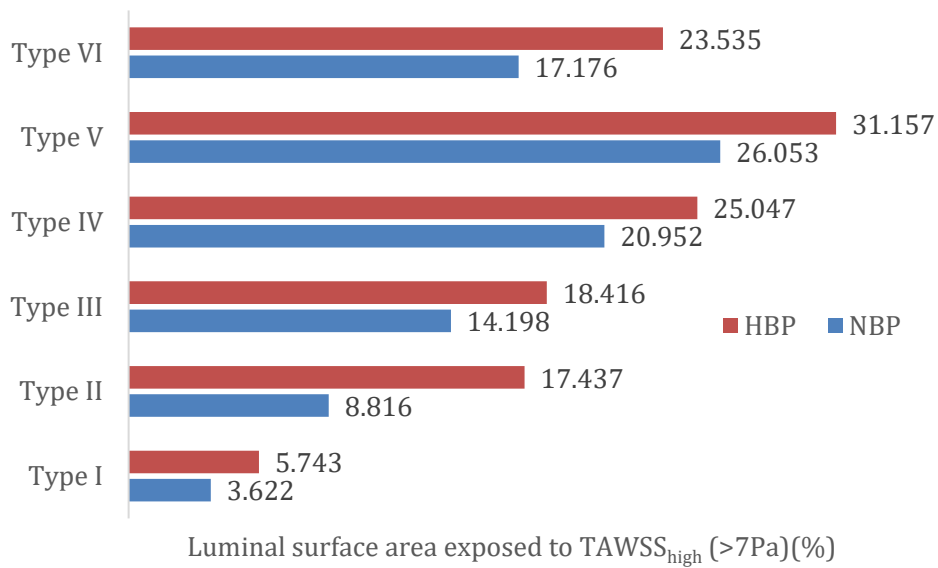


Figure 10: $TAWSS_{high}$ ($TAWSS > 7 \text{ Pa}$) distribution coverage to luminal surface area of carotid artery.

3.4 Time Averaged Wall Shear Stress Gradient (TAWSSG)

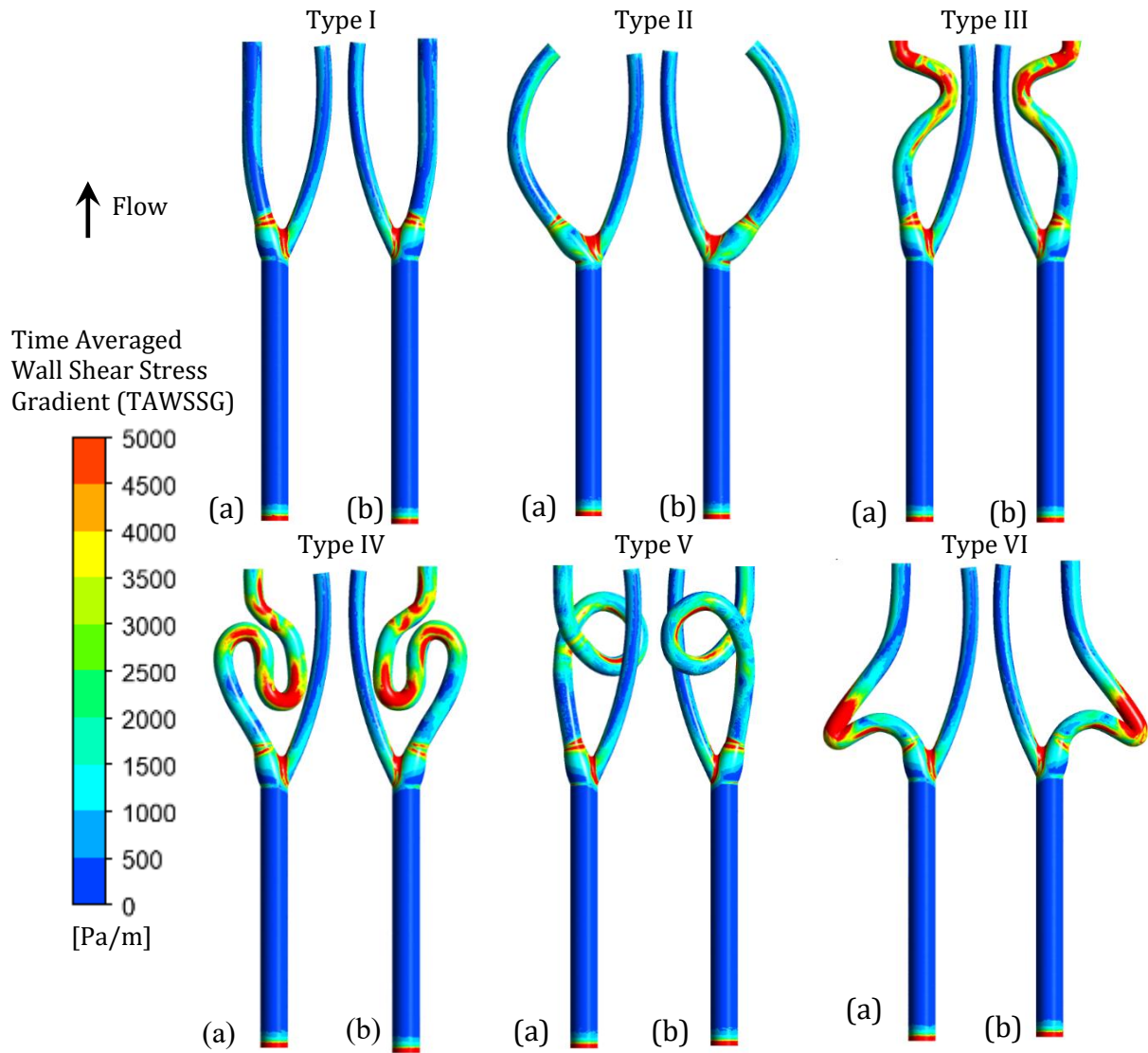


Figure 11: TAWSSG distribution at (a) anterior (b) posterior of healthy carotid artery for NBP condition.

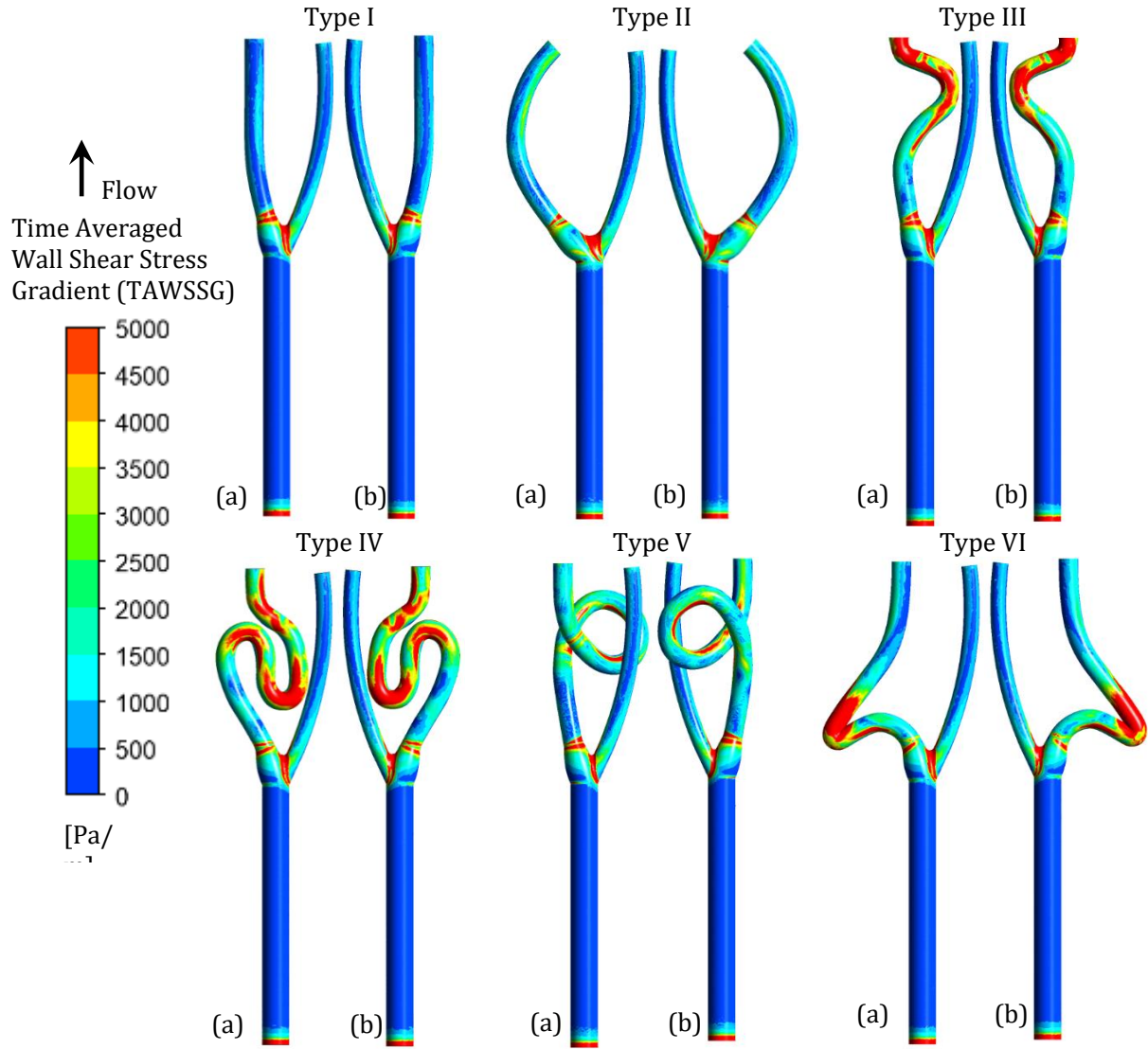


Figure 12: TAWSSG distribution at (a) anterior (b) posterior of healthy carotid artery for HBP condition.

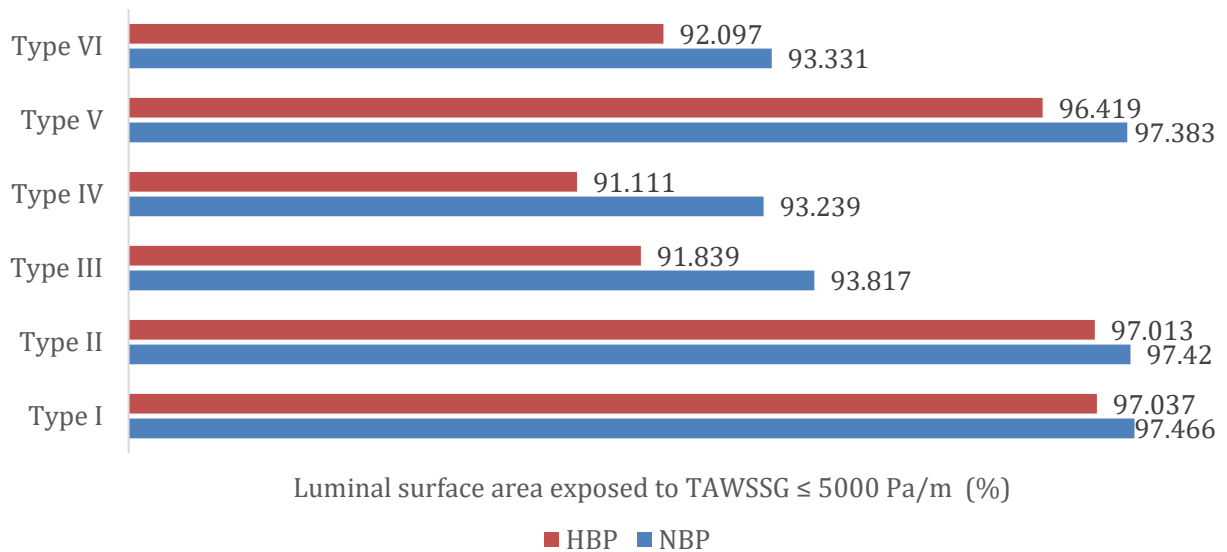


Figure 13: TAWSSG ≤ 5000 Pa/m distribution exposure to luminal surface area of healthy carotid artery.

Figures 11 and Figure 12 revealed that the HBP condition displayed a higher TAWSSG distribution (red) than the NBP condition. Figure 13 illustrated the calculated percentage luminal distribution exposed to TAWSSG ≤ 5000 Pa/m for better visualization. The TAWSSG value equal to and below 5000 Pa/m to has lower risk for the development of thrombosis. Type I and II showed the least luminal surface area exposed to TAWSSG. In contrast, the morphology exhibited by Type III, IV, V and VI carotid arteries demonstrated a high TAWSSG distribution at the sides of curvature and at the inner bending of ICA, whereas lower TAWSSG distribution (blue) was seen at the outer wall of bending. The TAWSSG result of the current simulation was aligned with a prior study done by Buradi and Mahalingam (2020), showing a comparable TAWSSG distribution at the arterial curvatures.

3.5 Oscillatory Shear Index (OSI)

The OSI distribution for carotid artery morphology at both physiological conditions is depicted in Figures 14 and Figure 15. The direction of shear stress change defined by OSI was due to the reduction in blood flow velocity, which resulted in regions of recirculating flow that promote the development of atherosclerosis (Lopes *et al.*, 2020; Soares, Carvalho & Leite, 2021; Lagache *et al.*, 2021). A high OSI value of more than 0.2 indicated significant blood flow oscillation, which aided in the development of atherosclerosis and thrombosis. In this study, the OSI parameter was observed to be high at the curvature and bending regions as well as at the sinus of the carotid artery. A previous study by Buradi and Mahalingam in 2020 attested that the haemodynamic parameter of OSI distribution with a value greater than 0.2 was found near the arterial curve with a bigger radius, thus, demonstrating the validity of the findings in the present study. Figure 16 showed the percentage value of OSI equal to and less than 0.2 for clearer perspective. Type I demonstrated the highest distribution of OSI ≤ 0.2 whereas Type V showed the opposite. Based

on this value, the area of recirculating flow in Type I is smaller compared to the other morphological types, indicating it has the lowest risk of atherosclerosis development.

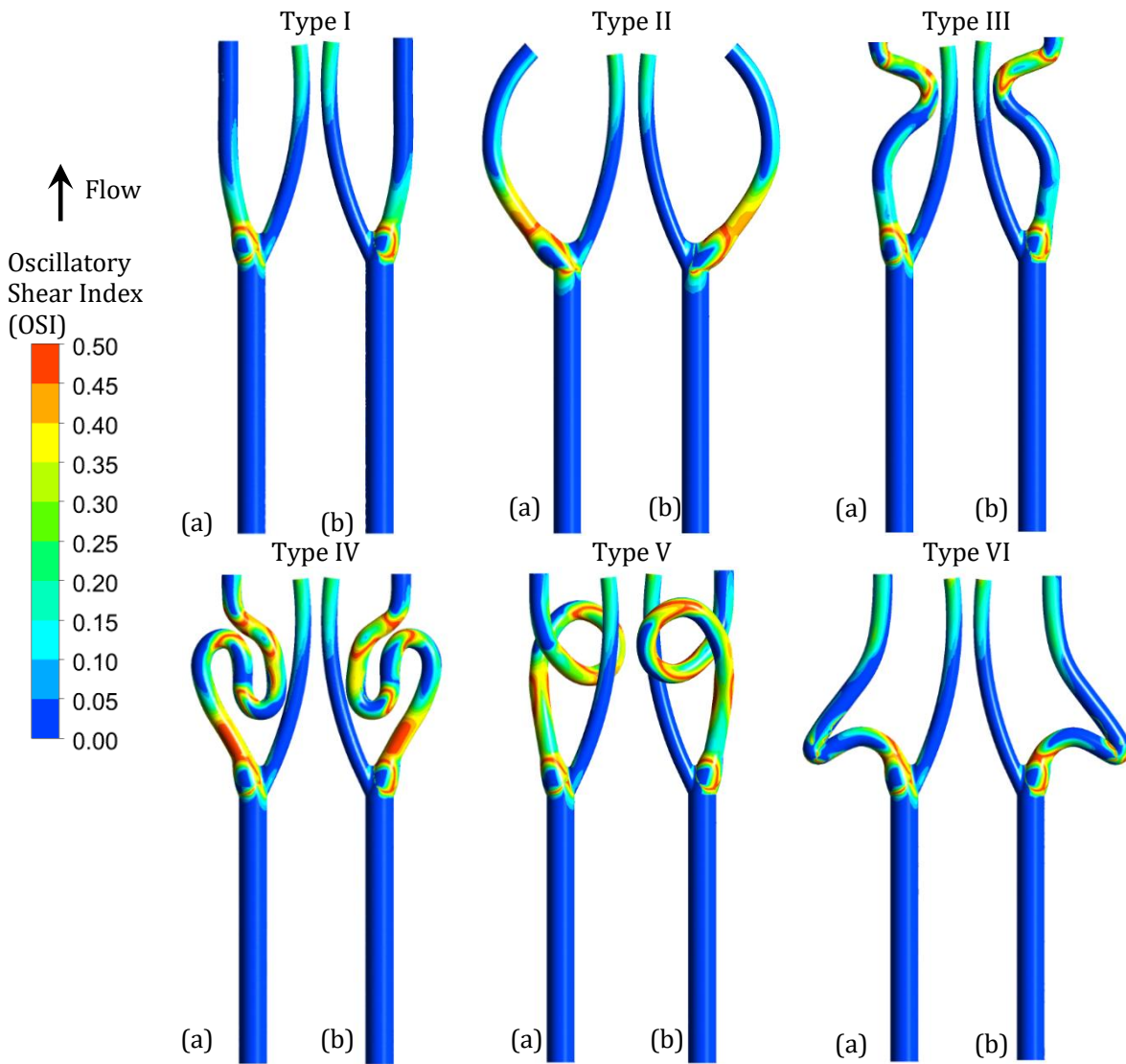


Figure 14: OSI distribution at (a) anterior (b) posterior of healthy carotid artery for NBP condition.

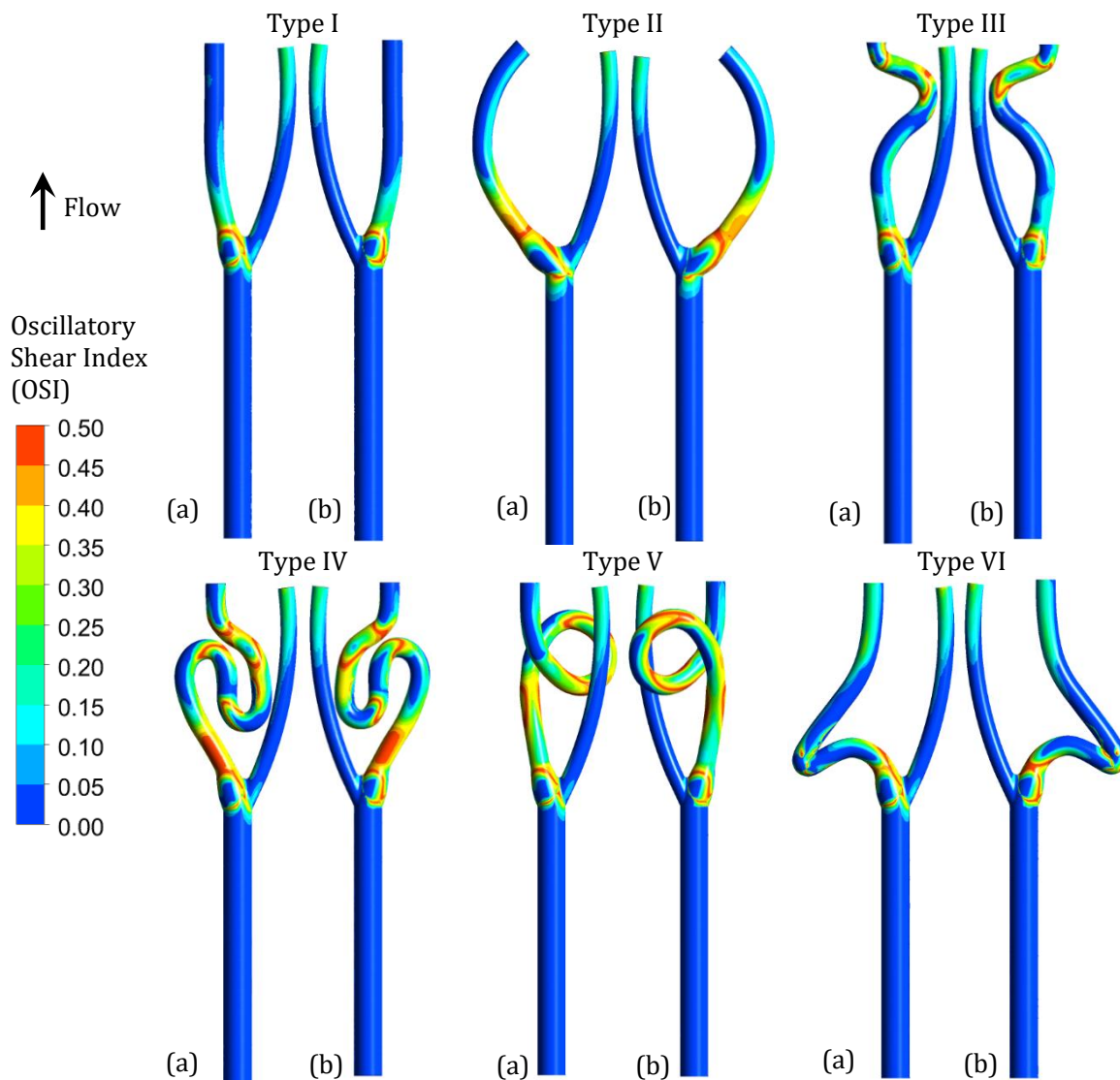


Figure 15: OSI distribution (a) anterior (b) posterior of healthy carotid artery for HBP condition.

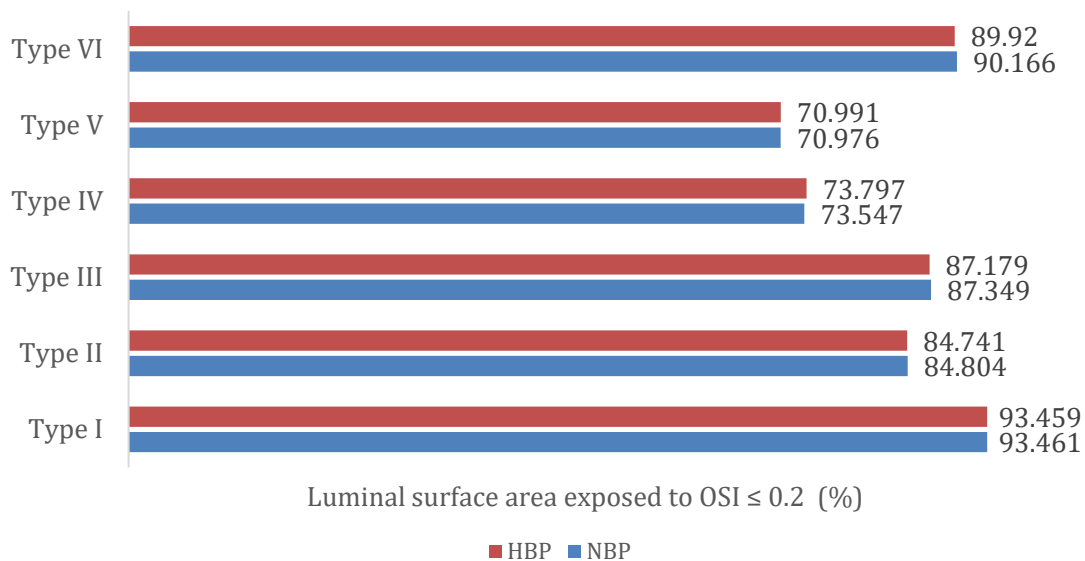


Figure 16: OSI \leq 0.2 distribution exposure to luminal surface area of carotid artery

3.6 Relative Residence Time (RRT)

As shown in Figures 17 and 18, the RRT distribution was greater than 10 Pa^{-1} (red) at the outer wall of the carotid sinus under both physiological conditions. The anterior and posterior exhibit a slight difference in RRT distribution due to the presence of carotid sinus. The variation of pulsatile flow profile entering the sinus result in asymmetrical flow behavior. Besides, prominent curvature and kink exhibited by Type III, IV, V and VI morphology displayed high RRT distribution at the outer wall of the bend. Greater RRT distribution values over 10 Pa^{-1} indicated that the particles and artery wall had been in contact for a longer period, which had a role in atherogenesis. This agrees with a previous study by Buradi and Mahalingam (2020) stated that the RRT showed a high distribution at the curvature of artery thus, validating the current findings.

In the presence of HBP condition, the carotid arteries showed a reduced distribution of RRT greater than 10 Pa^{-1} . As shown in Figure 19, HBP has a higher percentage of luminal surface area coverage to $\text{RRT} \leq 10 \text{ Pa}^{-1}$ compared to NBP condition. This result was comparable to that of the previous study by Paisal (2018), which discovered that when physiological condition increases from NBP to HBP, the luminal surface area covered by high RRT declined.

Furthermore, Type II carotid artery morphology has a smaller risk for stagnant atherogenic particles accumulation in comparison to other morphologies, whereas Type IV shown a higher possibility of atherogenic particles adhering to the arterial wall.

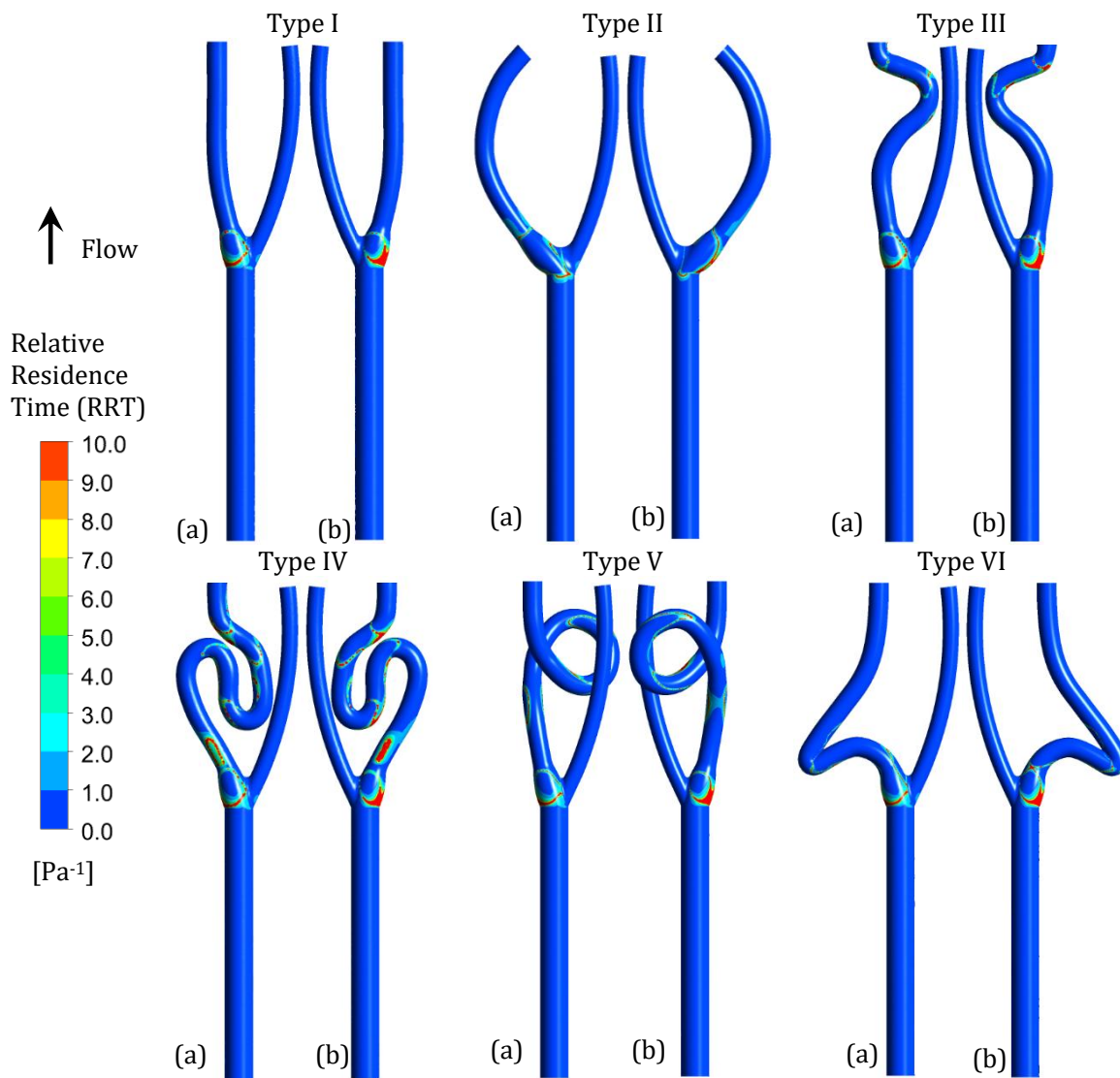


Figure 17: RRT distribution at (a) anterior (b) posterior of healthy carotid artery for NBP condition.

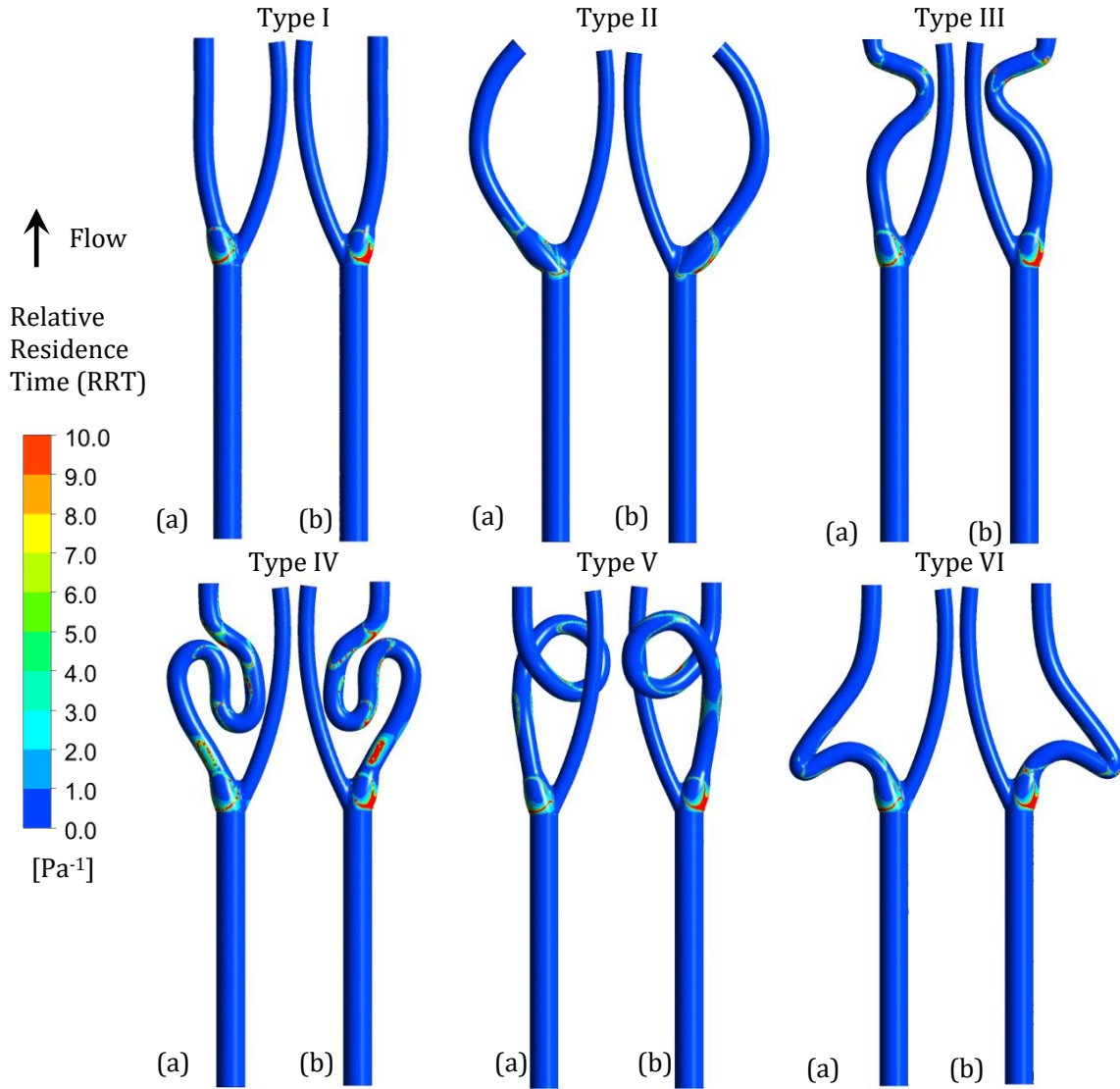


Figure 18: RRT distribution at (a) anterior (b) posterior of healthy carotid artery for HBP condition.

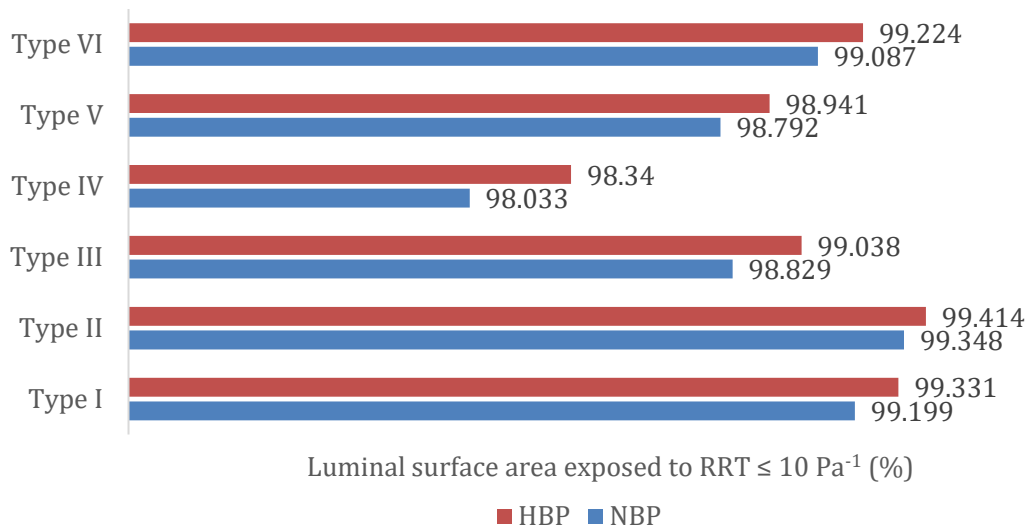


Figure 19: $RRT \leq 10 \text{ Pa}^{-1}$ distribution exposure to luminal surface area of carotid artery.

CONCLUSIONS

The different vascular geometry presented by the carotid artery has been recognized to affect the blood flow behavior. The misalignment of blood flow in the bifurcated carotid artery coupled with the vascular curving, twisting, looping, and kinking led to the region with blood flow recirculation. Physiological conditions exhibited have also been proven to further affect the hemodynamic behavior. Hence, the morphology coupled with physiological conditions exhibited by the carotid artery gives a significant influence on the risk of thrombosis growth leading to stenosis events. Therefore, these factors should be taken into thoughtful consideration for further diagnosis or medical intervention.

ACKNOWLEDGMENT

This research was supported by Universiti Tun Hussein Onn Malaysia (UTHM) through Multidisciplinary Research Grant (MDR) (vot Q686).

REFERENCES

- Aldoori, M.I., Lee, R.E. (1993). Carotid blood flow and pathogenesis of cerebral ischaemia. In: Salmasi, AM., Iskandrian, A.S. (eds) *Cardiac Output and Regional Flow in Health and Disease*. Dordrecht: Springer.
- Ayasamy, P. T. (2025). Integrating CFD Tools for the Simulation and Analysis of Turbulent Flow Dynamics in a Y-Junction Pipe. *Semarak Journal of Thermal Fluid Engineering*, 5(1), 46-54.
- Azar, D., Torres, W.M., Davis, L.A., Shaw, T., Eberth, J.F., Kolachalama, V.B., Lessner, S.M. & Shazly, T. (2019). Geometric determinants of local hemodynamics in severe carotid artery stenosis. *Computers in biology and medicine*, 114, 103436.

- Azhim, A., Sakagami, K., Ueno, A., Kinouchi, Y., & Fukui, Y. (2013). Independent factors of flow velocity indices in common carotid artery. In *World Congress on Medical Physics and Biomedical Engineering*. Beijing, China: Springer, 445-448.
- Balevi, M. (2020). Dolicho-Arteriopathies (Kinking, Coiling, Tortuosity) of the Carotid Arteries: A Study by Magnetic Resonance Angiography. *International Journal of Head and Neck Surgery*, 11(3), 50-54.
- Beigelman, R., Izaguirre, A., Azzato, F., & Milei, J. (2014). Carotid Artery–Pathology, Plaque Structure–Relationship between Histological Assessment, Color Doppler Ultrasonography and Magnetic Resonance Imaging–Dolichoarteriopathies–Barorreceptors. *Carotid artery disease—from bench to bedside and beyond*, 31-83.
- Bir, S. C., & Kelley, R. E. (2022). Carotid atherosclerotic disease: A systematic review of pathogenesis and management. *Brain circulation*, 8(3), 127-136.
- Buradi, A., & Mahalingam, A. (2020). Impact of coronary tortuosity on the artery hemodynamics. *Biocybernetics and Biomedical Engineering*, 40(1), 126-147.
- Campbell, B. C., De Silva, D. A., Macleod, M. R., Coutts, S. B., Schwamm, L. H., Davis, S. M., & Donnan, G. A. (2019). Ischaemic stroke. *Nature Reviews Disease Primers*, 5(1), 70.
- Carallo, C. (2019). Effect of ageing on carotid artery morphology, hemodynamics, and the development of atherosclerosis. Imperial College London.
- Carvalho, V., Pinho, D., Lima, R. A., Teixeira, J. C., & Teixeira, S. (2021). Blood flow modeling in coronary arteries: A review. *Fluids*, 6(2), 53.
- Datta, A., & Rakesh, V. (2010). An introduction to modeling of transport processes: applications to biomedical systems. Cambridge University Press
- Di Pino, L., Franchina, A. G., Costa, S., Gangi, S., Strano, F., Ragusa, M., Costanzo, L., Tamburino, C. and Capodanno, D. (2021). Prevalence and morphological changes of carotid kinking and coiling in growth: an echo-color Doppler study of 2856 subjects between aged 0 to 96 years. *The International Journal of Cardiovascular Imaging*, 37, 479-484.
- DiCarlo, A. L. (2018). Investigation of Flow Disturbances and Multi-Directional Wall Shear Stress in the Stenosed Carotid Artery Bifurcation Using Particle Image Velocimetry (Doctoral dissertation, The University of Western Ontario (Canada)).
- Everson-Rose, S. A., & Fordham, K. M. (2022). Stroke and Carotid Artery Disease. In *Handbook of Cardiovascular Behavioral Medicine*. New York, NY: Springer New York, 1207-1226.
- Ghani, J.A., Guoliang, Y., Hamran, N.N.N., Yap, P.H., Rahman, H.A., Mahmood, W.M.F.W., Ramli, R., Ni, J. and Iqbal, U.M. (2023). Simulation Study of the parameters that affecting the droplets size produced in a Minimum Quantity Lubrication (MQL) system using a Computational Fluid Dynamic (CFD). *Jurnal Tribologi*, 36, 116-126.
- Hameed, M. S., Shah, A. A., Khan, M. I., Ali, A., Hussain, I., & Bukhari, M. D. (2023). Comparison of blood flow analysis in stenosed and stented carotid artery bifurcation models. *Cogent Engineering*, 10(1), 2158624.
- Hidayat, T., Ismail, R., Tauviqirrahman, M., Saputra, E., Ammarullah, M.I., Lamura, M.D.P., Bayuseno, A. and Jamari, J. (2023). Investigation of mesh model for a finite element simulation of the dual-mobility prosthetic hip joint. *Jurnal Tribologi*, 38, 118-140.
- Huang, Y. X., Mahler, S., Abedi, A., Tyszka, J. M., Lo, Y. T., Lyden, P. D., Russin, J., Liu, C. and Yang, C. (2024). Correlating stroke risk with non-invasive tracing of brain blood dynamic via a portable speckle contrast optical spectroscopy laser device. *arXiv preprint arXiv:2407.16571*.

- Ibrahim, N., Roseman, N. A. H., Taib, I., & Shanta, S. (2024). CFD Based on The Visualisation of Aortic Valve Mechanism in Aortic Valve Stenosis for Risk Prediction at The Peak Velocity. *Journal of Advanced Research in Micro and Nano Engineering*, 17(1), 56-68.
- Iomini, P. A., Beigelman, R., Ambrosio, G., Izaguirre, A., & Milei, J. (2024). Carotid Dolichoarteriopathies: A Comprehensive Overview. *Revista argentina de cardiología*, 92(3), 239-246.
- Katakia, Y. T., Kanduri, S., Bhattacharyya, R., Ramanathan, S., Nigam, I., Kuncharam, B. V. R., & Majumder, S. (2022). Angular difference in human coronary artery governs endothelial cell structure and function. *Communications Biology*, 5(1), 1044.
- Khalili, F., Gamage, P., & Mansy, H. A. (2018). Verification of turbulence models for flow in a constricted pipe at low reynolds number. *arXiv preprint arXiv:1803.04313*.
- Kok, A.M., Molony, D.S., Timmins, L.H., Ko, Y.A., Boersma, E., Eshtehardi, P., Wentzel, J.J. & Samady, H. (2019). The influence of multidirectional shear stress on plaque progression and composition changes in human coronary arteries. *EuroIntervention*, 15(8), 692-699.
- Krishnamurty, D. (2025). Simulation of Tapered Pipe Turbulent Flow in Various Internal Flow Geometries. *Journal of Advances in Fluid, Heat, and Materials Engineering*, 5(1), 1-9.
- Kumar, N., Khader, S. A., Pai, R., Khan, S. H., & Kyriacou, P. A. (2020). Fluid structure interaction study of stenosed carotid artery considering the effects of blood pressure. *International Journal of Engineering Science*, 154, 103341.
- Kumar, N., Pai, R., Abdul Khader, S. M., Khan, S. H., & Kyriacou, P. A. (2022). Influence of blood pressure and rheology on oscillatory shear index and wall shear stress in the carotid artery. *Journal of the Brazilian Society of Mechanical Sciences and Engineering*, 44(11), 510.
- Lagache, M., Coppel, R., Finet, G., Derimay, F., Pettigrew, R. I., Ohayon, J., & Malvè, M. (2021). Impact of malapposed and overlapping stents on hemodynamics: a 2D parametric computational fluid dynamics study. *Mathematics*, 9(8), 795.
- Lopes, D., Puga, H., Teixeira, J., & Lima, R. (2020). Blood flow simulations in patient-specific geometries of the carotid artery: A systematic review. *Journal of Biomechanics*, 111, 110019.
- Masibayi, A. (2011). Application of The Navier-stokes Equations In The Localisation Of Atherosclerosis, University of Nairobi, Kenya: Doctoral dissertation.
- Mendieta, J. B., Fontanarosa, D., Wang, J., Paritala, P. K., McGahan, T., Lloyd, T., & Li, Z. (2020). The importance of blood rheology in patient-specific computational fluid dynamics simulation of stenotic carotid arteries. *Biomechanics and Modeling in Mechanobiology*, 19(5), 1477-1490.
- Metz, H., Bannister, R. G., Murray-Leslie, R. M., Bull, J. W. D., & Marshall, J. (1961). Kinking Of The Internal Carotid Artery: in Relation to Cerebrovascular Disease. *The Lancet*, 277(7174), 424-426.
- Nagata, T., Masumoto, K., Hayashi, Y., Watanabe, Y., Kato, Y., & Katou, F. (2016). Three-dimensional computed tomographic analysis of variations of the carotid artery. *Journal of Cranio-Maxillofacial Surgery*, 44(6), 734-742.
- Paisal, M. S. A. (2018) Computational analysis on stent geometries in carotid artery. (Universiti Tun Hussein Onn Malaysia: Masters thesis).
- Paisal, M. S. A., Taib, I., Arifin, A. M. T., & Mahmud, M. F. (2019). Evaluation system on haemodynamic parameters for stented carotid artery: Stent pictorial selection method. *International Journal of Integrated Engineering*, 11(1).
- Pal, S. C., Kumar, M., & Dayal, R. (2022). A comparative study of patient-specific bifurcated carotid artery with different viscosity models. In *Application of Soft Computing Techniques in Mechanical Engineering*. CRC Press, 215-230.

- Pedley, T. (2022). Blood Flow. *Blood*, 38-62.
- Pinho, N., Sousa, L.C., Castro, C.F., António, C.C., Carvalho, M., Ferreira, W., Ladeiras-Lopes, R., Ferreira, N.D., Braga, P., Bettencourt, N. & Pinto, S.I.S. (2019). The impact of the right coronary artery geometric parameters on hemodynamic performance. *Cardiovascular engineering and technology*, 10, 257-270.
- Rabbi, M. F., Laboni, F. S., & Arafat, M. T. (2020). Computational analysis of the coronary artery hemodynamics with different anatomical variations. *Informatics in Medicine Unlocked*, 19, 100314.
- Roseman, N. A. H. B. (2023). Analysis of Flow Disturbance Due to Stenosed Carotid Artery Wall (Master's thesis, Universiti Tun Hussein Onn (Malaysia)).
- Sambu, M., Zaman, I., Manshoor, B., Nagentrau, M., Tai, V.C. (2024). Numerical Study of Vortex Effect on Splitter Plate under Turbulence Flow over Circular Cylinder. *Journal of Advanced Mechanical Engineering Applications*, 5(1), 36-45.
- Santos, S., Rojas, J. M., Romero, P., Lozano, M., Conejero, J. A., & García Fernández, I. (2021). Analysis of turbulence models for flow simulation in the aorta. In *Proceedings of the XXVI Congreso de Ecuaciones Diferenciales y Aplicaciones. XVI Congreso de Matemática Aplicada*. Servicio de Publicaciones de la Universidad de Oviedo.
- Saqr, K. M., Tupin, S., Rashad, S., Endo, T., Niizuma, K., Tominaga, T., & Ohta, M. (2020). Physiologic blood flow is turbulent. *Scientific reports*, 10(1), 1-12.
- Saufi, O. M. M., Roseman, N. A. H. B., Taib, I., Nasir, N. F., Ariffin, A. M. T., Salim, N. A. N., Osman, S. A., Darlis, N. I. and Kareem, A. K. (2023). Flow Characteristics on Carotid Artery Bifurcation of Different Aneurysmal Morphology. *CFD Letters*, 15(2), 25-40.
- Sia, S. F., Zhao, X., Yu, Y., & Zhang, Y. (2019). Multiphase particle-in-cell simulation in severe internal carotid artery stenosis. *Powder Technology*, 358, 62-67
- Sjöstrand, S., Widerström, A., Svensson, I., Segers, P., Erlöv, T., Ahlgren, Å. R., & Cinthio, M. (2023). The impact of geometry, intramural friction, and pressure on the antegrade longitudinal motion of the arterial wall: A phantom and finite element study. *Physiological Reports*, 11(12), e15746.
- Soares, A., Carvalho, F., & Leite, A. (2021). Wall Shear Stress-Based Hemodynamic Descriptors in the Abdominal Aorta Bifurcation: Analysis of a Case Study. *Journal of Applied Fluid Mechanics*, 14(6), 1657-1668.
- Weibel, J., & Fields, W. S. (1965a). Tortuosity, coiling, and kinking of the internal carotid artery: II. Relationship of morphological variation to cerebrovascular insufficiency. *Neurology*, 15(5), 462-462.
- Weibel, J., & Fields, W. S. (1965b). Tortuosity, coiling, and kinking of the internal carotid artery: I. Etiology and radiographic anatomy. *Neurology*, 15(1), 7-7.
- Yao, X., Dai, Z., Zhang, X., Gao, J., Xu, G., Cai, Y., & Li, Z. (2019). Carotid Geometry as a Predictor of In-Stent Neointimal Hyperplasia—A Computational Fluid Dynamics Study—. *Circulation Journal*, 83(7), 1472-1479.
- Yu, Z., Tan, J., & Wang, S. (2021). Enhanced discrete phase model for multiphase flow simulation of blood flow with high shear stress. *Science Progress*, 104(1), 00368504211008064.
- Zhong, S. Z., & Kong, J. M. (1989). *Microsurgical anatomy in China*. *Surgical and Radiologic Anatomy*, 11(2), 115-122.
- Zulkifli, Z., Halim, N. H. A., Solihin, Z. H., Saedon, J., Ahmad, A. A., Raof, N. A., & Hadi, M. A. (2023). Validation of MQL delivery system through simulation by computational fluid dynamics (CFD) analysis. *Jurnal Tribologi*, 37, 98-112.